Fire resistance of composite steel & concrete highway bridges

Fire resistance of composite steel & concrete highway bridges

Jiayu Hu[a, *], Asif Usmani[b], Abdel Sanad[c], Ricky Carvel[a]

[a] Institute for Infrastructure and Environment, School of Engineering, The University of Edinburgh, Edinburgh EH9 3JF, UK.

[b] Department of Building Services Engineering, Faculty of Construction and Environment, The Hong Kong Polytechnic University, Kowloon, Hong Kong.

[c] Construction and Building Department, Faculty of Engineering & Technology, The Arab Academy for Science, Technology and Maritime Transport, Cairo, Egypt.

*Corresponding author. Email address: Jiayu.Hu@ed.ac.uk

ABSTRACT

In this paper, the effects of geometric skewness and abutment restraint on the fire resistance of a real highway bridge have been studied. Four finite element models have been investigated using rectangular and skew shapes with and without modelling the abutment. The investigation has been carried out in three steps: 1) heat transfer analysis under a specified hydrocarbon fire; 2) simulation of the thermo-mechanical response of the bridge superstructure over the entire duration of the fire using beam and shell elements to represent the structural components; 3) detailed processing and interpretation of the simulation results to understand and illustrate the global response of the structure by comparing all the models. Results indicate that a skew bridge may possess greater inherent resistance to fire. For the two-span highway bridge model, restraint from the abutment does not affect the estimated failure time significantly.

Keywords: Performance-based engineering, bridges in fire.

1. INTRODUCTION

Bridge fire hazard is typically associated with vehicle fire incidents, which have a relatively low-probability of occurrence. However these incidents may sometimes lead to severe consequences such as structural damage to bridges and the consequent economic losses due to transport network disruptions. A survey from the New

York State Department of Transportation found that nearly three times as many bridges collapsed between 1990 and 2005 because of fires against those due to earthquakes [1].

Unlike building and tunnel fires, which have been studied for decades (e.g. Carvel *et al.* [2], Flint *et al.* [3], Lange *et al.* [4], Lamont *et al.* [5]), the impact of fire hazard on bridges has not received much attention to date. There are also currently no requirements under building or highway codes to consider the fire resistance of bridges, which the authors feel is a grave omission, considering the enormous risk to economic and social stability that disruption of a major artery of the transport network may represent.

A preliminary assessment of the most at risk bridges in a network may be determined based on the review of incidents and accidents in the past. Often vehicle fire incidents occur without causing much damage, especially when the accident occurs on top of the bridge deck (e.g. HGV fire on the A9 at Slochd Rail Bridge [6]). However, there have been numerous vehicle fires that have occurred underneath bridge superstructures leading to severe structural damage [7,8]. In 2004, a car collided with a tanker truck on the Wiehlthal Bridge on the A4 motorway in Germany, causing the truck to fall 100ft followed by a fire underneath the bridge structure. This severe incident caused major structural damage, which resulted in a cost of $42 million just for temporary repairs to restore traffic flows and $400 million in total economic losses [9]. In another accident in 2009, when a speeding driver hit a fuel tanker with 13,000 gallons of fuel, causing the tanker to impact into a column supporting the 9 Mile Road Bridge in the city of Hazel Park, Michigan. The tanker burst into flames under the bridge resulting in the collapse of one span and a loss of many millions of dollars [10].

In the past five years, several researchers have investigated structural behaviour of bridge components under fire loading by performing finite element models or experiments, mainly on a single composite girder [1,11–13]. Parameters affecting failure time/mode such as web slenderness and spacing of stiffeners have been studied. However, the estimated failure time and failure mode of a single component is questionable to

represent the failure behaviour of a whole bridge frame. Therefore, some other researchers [14–16] have simulated full-scale bridges and performed a 6m span bridge test in Valencia [17]. In these studies, certain key factors which may affect bridge fire resistance have been discussed, including fire intensity, fire positions, exposure scenarios, material types, live loads and wind.

This paper progresses the previous work in a number of ways. Most importantly we present a thorough computational analysis of a composite steel framed bridge superstructure subjected to a large fire to investigate the effect of bridge shape, considering that skew bridge shapes are quite commonly used. A collapse mechanism and failure phases specifically for bridges are clearly defined based on a well-defined criterion without recourse to ad-hoc considerations of deflections or deflection rates. In assessing the eventual failure of the bridge, detailed descriptions of the thermo-mechanical response is presented as we have not found this kind of insight in existing literature. Composite behaviour has also been included, considering composite structural components experience thermal elongation and thermal bowing because of the heating from the fire. Thermal bowing induced rotation may cause the bridge superstructure to impinge upon the abutment due to its significant depth, therefore this effect has also been considered in the modelling.

The structural system of the bridge chosen for analysis is based on a representative bridge type commonly found on the UK highway network and therefore the findings of the work should have significant practical relevance. The insights presented here should help engineers to propose improved bridge structural systems and enable innovative design of structural elements to improve the inherent fire resistance of a composite steel and concrete bridge superstructure.

Published in Journal of Constructional Steel Research, June 2018. doi.org/10.1016/j.jcsr.2018.06.021

2. THE STIRLINGSHIRE LINK MOTORWAY BRIDGE

The models presented in this paper are based on the Stirlingshire Link Motorway Bridge (see Figure 1), which is located near Falkirk, UK. This bridge was constructed in 1980 [18], in order to connect the M9 and M876 motorways.

The structural framing is a skew two-span steel grillage consisting of 1.1m deep welded plated girder with internal diaphragms, supporting a 300mm deep top slab which forms the carriage way. The spread footings on rock foundation provide three supports for the bridge. Two end supports are full height cantilever abutments, and the intermediate support is a solid wall pier. Transverse diaphragms are placed between the webs of the steel girders, which play an important role in the lateral stability of bridge girders and in evening out the distribution of the dead and imposed loads.

(a) (b)

Figure 1. The Stirlingshire link motorway bridge [18]: (a) looking downlink on M9; (b) detail view of steelwork typical.

The original design of the bridge was provided by Transport Scotland, showing that the bridge consists of six primary beams with lengths 57.975m, 56.870m, 55.767m, 54.666m, 53.572m and 52.480m respectively. The primary beams are not exactly parallel to each other and the distance between concrete diaphragms also varies. The models used in this study are based on this bridge, however with simplified dimensions actually used as described in detail in Section 4.1.

Published in Journal of Constructional Steel Research, June 2018. doi.org/10.1016/j.jcsr.2018.06.021

3. THERMAL ANALYSIS

To determine the impact of the fire on the bridge superstructure, a heat transfer analysis is first required in order to define the equivalent thermal regime to be applied to the structural models. A nominal fire curve, namely the hydrocarbon fire [19], is used to perform a 2D uncoupled transient heat transfer analysis using Abaqus 6.12. The bridge is assumed to suffer a vehicle fire for 20 min, which could potentially result from a fuel tanker accident under the central girder of Span 2 (fire affected span, FAS, see Figure 5). The 20 min fire duration is assumed based on a review of real bridge fire accidents [1], which suggests that failure/collapse occurred at that level of exposure.

According to the drawings, the fire and hot smoke should be able to spread to Span 1 through the gap between top pier and steel sections. However, in this paper, Span 1 (non-fire affected span, NFAS, see Figure 5) is assumed to be insulated from the fire due to heat shielding effect of the central solid pier.

3.1 MODEL DESCRIPTION

The element DC2D4 was employed to construct the heat transfer models, which is a 4-node linear diffusive heat transfer quadrilateral element. The adopted size of mesh and discretization can be seen in Figure 2, in which 1680 and 3900 elements are used to model the primary composite beam and the concrete transverse diaphragm respectively. A non-uniform mesh has been used in concrete slab, where more elements are used above the steel section to better capture the heat transfer between the concrete and steel. A mesh sensitivity study was performed by comparing the heat transfer results between the primary beam model using only 420 elements and 1680 elements. It produces identical results which prove that even the coarser mesh is adequate for this study (Figure 3). In the heat transfer models, the exposed surfaces of both sections received the incident heat flux through the mechanisms of convection and radiation, while the slab is assumed to be

heated from the bottom only. The upper unexposed surface of the slab is allowed to lose heat by convection and radiation to ambient air.

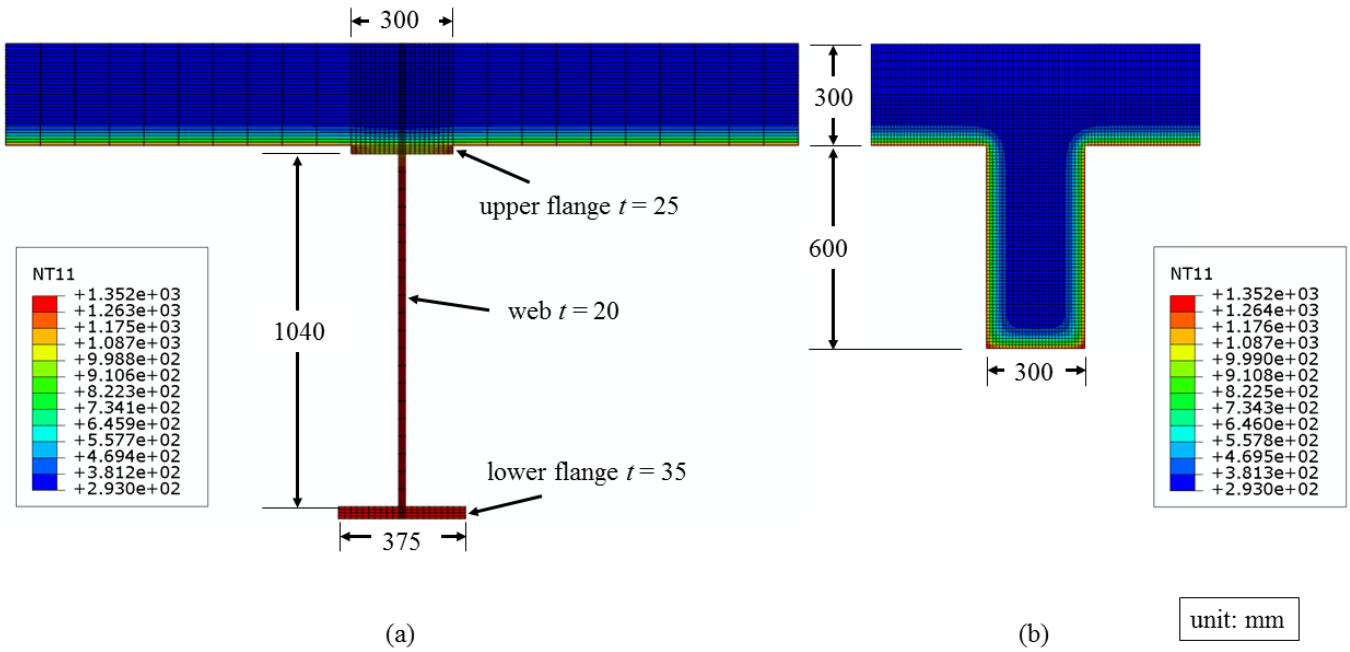

Figure 2. Heat transfer model at 20 min: (a) primary beam, (b) transverse diaphragm. All temperatures are given in K.

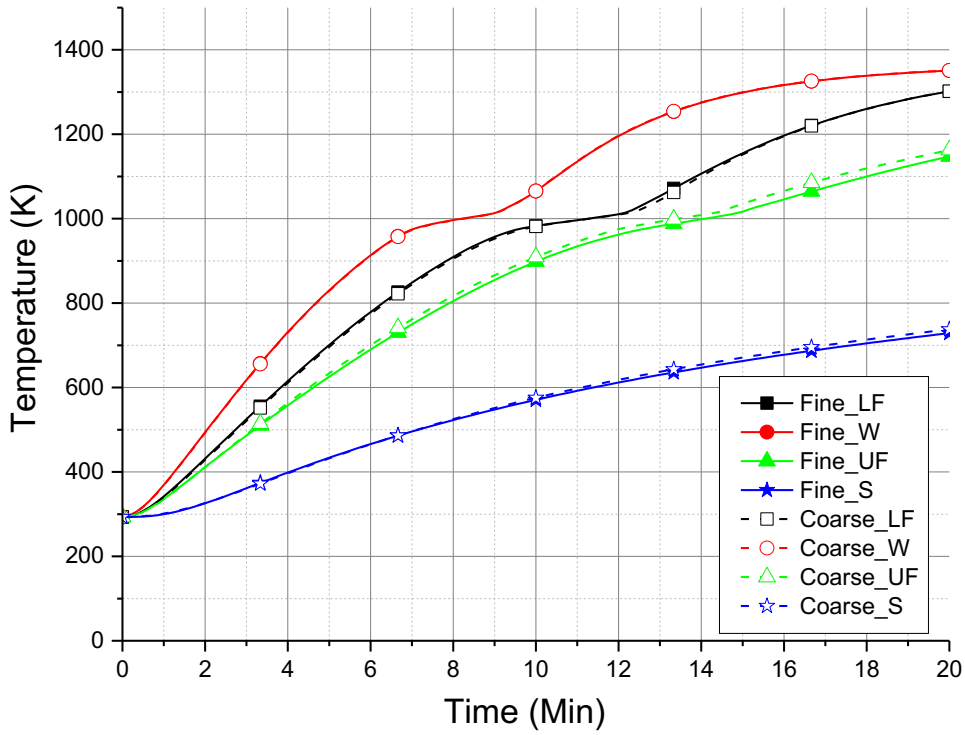

Figure 3. Primary beam model heat transfer results using fine mesh (1680 elements) and coarse mesh (420 elements).

Isotropic thermal conductivity and specific heat are used for both steel and concrete and assumed to vary with temperature in accordance with Eurocode [20,21]. The upper limit of thermal conductivity of normal weight concrete composed of siliceous aggregate was adopted in the study for a more conservative result as calcareous aggregate concrete has better performance in terms of residual strength at elevated temperatures.

Radiation and convection boundary conditions were specified for both the fire-exposed and unexposed surfaces of the structure. The convection coefficient [22] was set to $50\ W/(m^2K)$ for fire-exposed surfaces under hydrocarbon fire and $4\ W/(m^2K)$ for the unexposed surfaces. Some of the literature studies [11] use $25\ W/(m^2K)$ for the unexposed surfaces which should also be reasonable as this paper performed a sensitivity study and proves that no differences are caused by the value of convective coefficient used for the slab top. This is due to the thick depth (300 mm in this paper) of a bridge deck. An effective emissivity factor of 0.7 was used for both concrete and steel at all surfaces[20,21].

3.2 HEAT TRANSFER ANALYSIS

The temperature variation along the composite section is determined as a function of fire exposure time from the heat transfer analysis as shown in Figure 4. As expected, the temperature in concrete is significantly lower than that in the steel section due to its lower thermal conductivity. Also, the steel web heats up at a much higher rate compared to the flanges due to its smaller thickness. The upper flange has a lower temperature because of the heat loss to the adjacent concrete slab. However, because of the high thermal conductivity of steel, the temperatures at different positions in the steel section would tend to approach the same value after about 30 min exposure (not shown in Figure 4 as this is beyond the time of interest in this analysis).

Published in Journal of Constructional Steel Research, June 2018. doi.org/10.1016/j.jcsr.2018.06.021

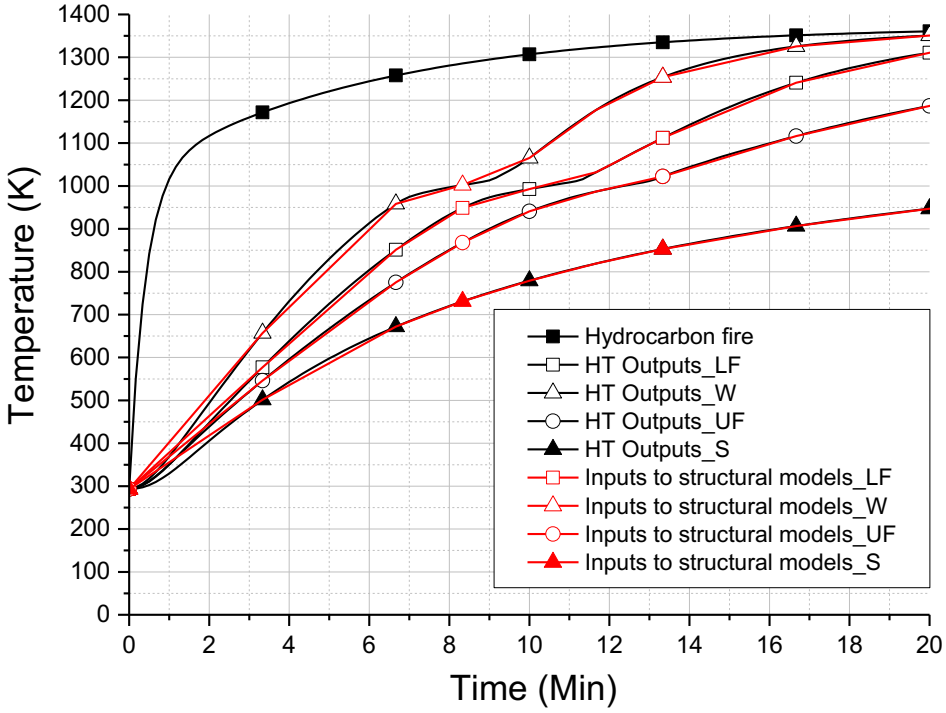

Figure 4. Temperature evolution with time within the composite section, comparison of heat transfer analysis and structural model inputs.

The output temperature variations from the heat transfer analysis were applied to the structural model using smaller time steps, in order to apply the thermal loading regime with small increments. As shown in Figure 4, the temperature profile applied to the structural model is sufficiently close to that obtained from the heat transfer analysis and should produce an acceptable simulation of the structural response.

4. STRUCTURAL MODELS

The models included the definition of structural members, material properties, boundary conditions, mechanical and thermal loadings and the structural analysis took into account geometric and material nonlinearities, as discussed below.

4.1 GEOMETRY

In order to investigate the influence of bridge shape and abutment restraint, four sets of discretised models have been built to conduct thermo-mechanical analysis, using rectangular or skew models with and without the modelling of abutment restraint.

The dimensions of the skew bridge based on the drawings were regularised (see Figure 5a) to obtain more generic results. Five primary beams were used to capture the behaviour of the central region of the structure accurately. All the beams have identical lengths of 57.6m (from North to South, namely BEAM No.1 to BEAM No.5) and the distance between primary beams and transverse diaphragms are kept constant at 3m and 4.8m respectively.

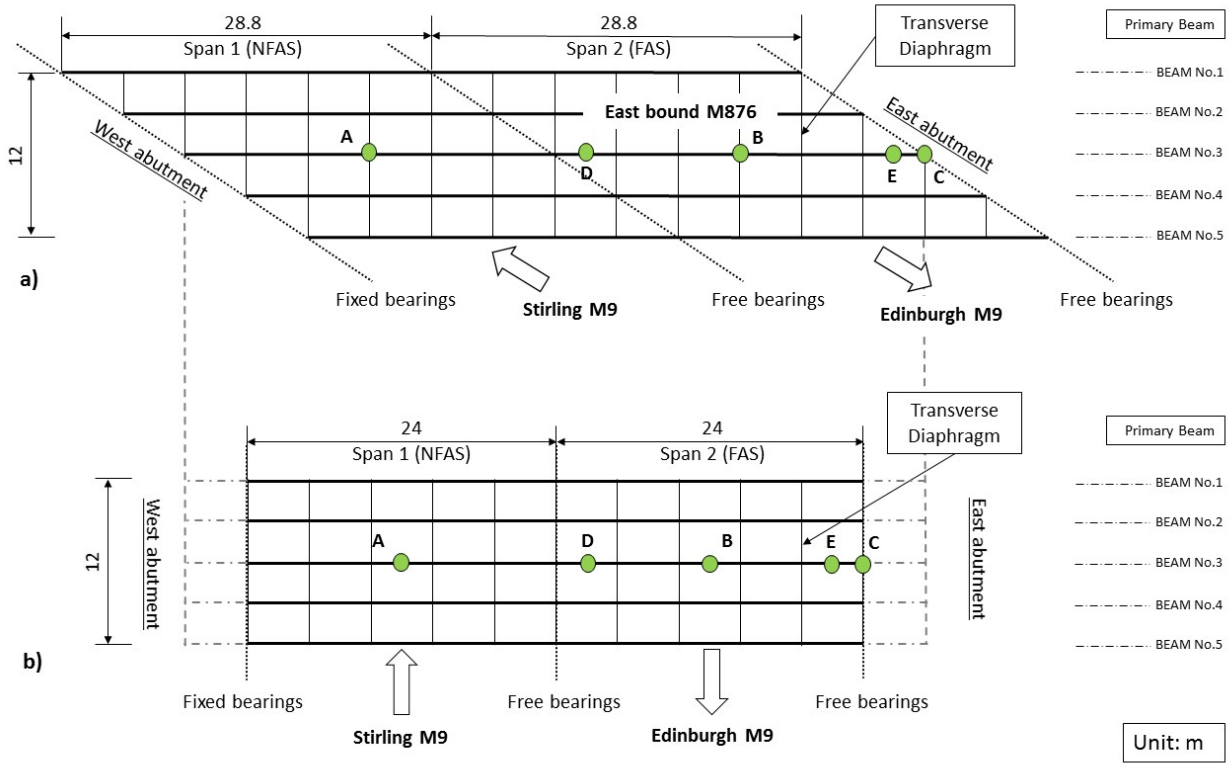

Figure 5. Schematic representations of the skew (a) and rectangular grillage (b).

The rectangular models were studied in order to establish the baseline structural behaviour of a similar span non-skew bridge. However, it is not possible to perform a like-for-like comparison of a rectangular bridge with a skew shape bridge as there is no clear equivalence between these two very different structural systems with significantly different structural behaviour. Estimation of an equivalent span length in a rectangular bridge is difficult as the effective span length in a skew shape bridge is not well defined. However, we feel that it is important to establish the reference behaviour of a somewhat similar rectangular bridge to understand the skew bridge behaviour better.

The rectangular bridge plan was defined to be consistent with skew bridge with a grillage framework composed of primary universal beams and transverse diaphragms arranged in a 48m x 12m grid (Figure 5b). Like the skew shape, the distance between primary beams and transverse diaphragms was defined as 3m and 4.8m respectively. A total length of 48m (based on 4 diaphragms spaced 4.8m apart in each span) was assumed for the rectangular bridge models compared to 57.6m (6 diaphragm spacings per span) for the skew bridge models. This is relatively arbitrary but a conservative estimation for comparison purposes. Using the same beam length in both shapes (as the extended dash dot lines show in Figure 5b would obviously make the rectangular bridge too weak compared to the skew bridge because the rectangular bridge can only carry loads in one-way bending. The skew shape provides additional capacity because of the contribution from two-way bending and the intrinsically stiffer behaviour from the reserves due to torsional serviceability requirements. Therefore, a shorter span has been used for the rectangular bridge to allow for some equivalence, but as mentioned earlier, this is not a like-for-like comparison but simply a device to provide a contrast or reference to understand the skew bridge behaviour better.

4.2 FINITE ELEMENT MODELS

The models were developed as a superstructure made out of a grillage of steel beams and concrete diaphragm acting compositely, with the concrete shell representing the carriageway. Only structural elements (beam

and shell element) are used in the models because: 1) local behaviour is not considered in this paper which is appropriate for establishing an upper bound reference global response; 2) to demonstrate the utility of a relatively low cost analysis that would be of interest to practicing engineers considering this problem, in fact for most bending dominated problems beam and shell elements are much more efficient and accurate than solid elements [23]; 3) Based on SCI steel and composite bridge structures report [24], the girders in the models will fail by yielding (275 MPa) rather than flange or web buckling (theoretical critical stress is 2136.51 MPa and 1597.71 MPa, see calculations below). It is also noted in [11] that *"steel bridge girders fail through flexural yielding when web slenderness is around 50"* (web slenderness is 52 in this paper).

$$\sigma_{cr} = \frac{k\pi^2 D}{td^2} = \frac{k\pi^2 E}{12(1-v^2)(\frac{d}{t})^2} \qquad \text{Eq. (1)}$$

(1) Buckling of web:

Web slenderness d/t = 52, k= 23.9. $\sigma_{cr} = 1597.71$ MPa.

(2) Buckling of compression flange:

Flange slenderness d/t = 6, k= 0.4255. $\sigma_{cr} = 2136.51$ MPa.

Each finite element in the model represents a discrete segment of the beams and slab. The B31 element was used for the primary beams and transverse diaphragms, which is a first-order, 2-node linear Timoshenko beam allowing for transverse shear deformation. For a more realistic and rigorous structural representation of concrete slab, the shell element S4R was adopted which is a 4-node, quadrilateral, stress/displacement shell element with reduced integration and a large-displacement formulation.

Reinforcement has been included in the slabs as a smeared layer of steel with the sectional area running through the slab. According to the drawings, the diaphragm steel is threaded through predrilled holes in the steel web of the beams. The steel in the diaphragm is included in the models. The undeformed view of the rectangular and skew models (with and without the abutment) with rendered section profiles are shown in Figure 6.

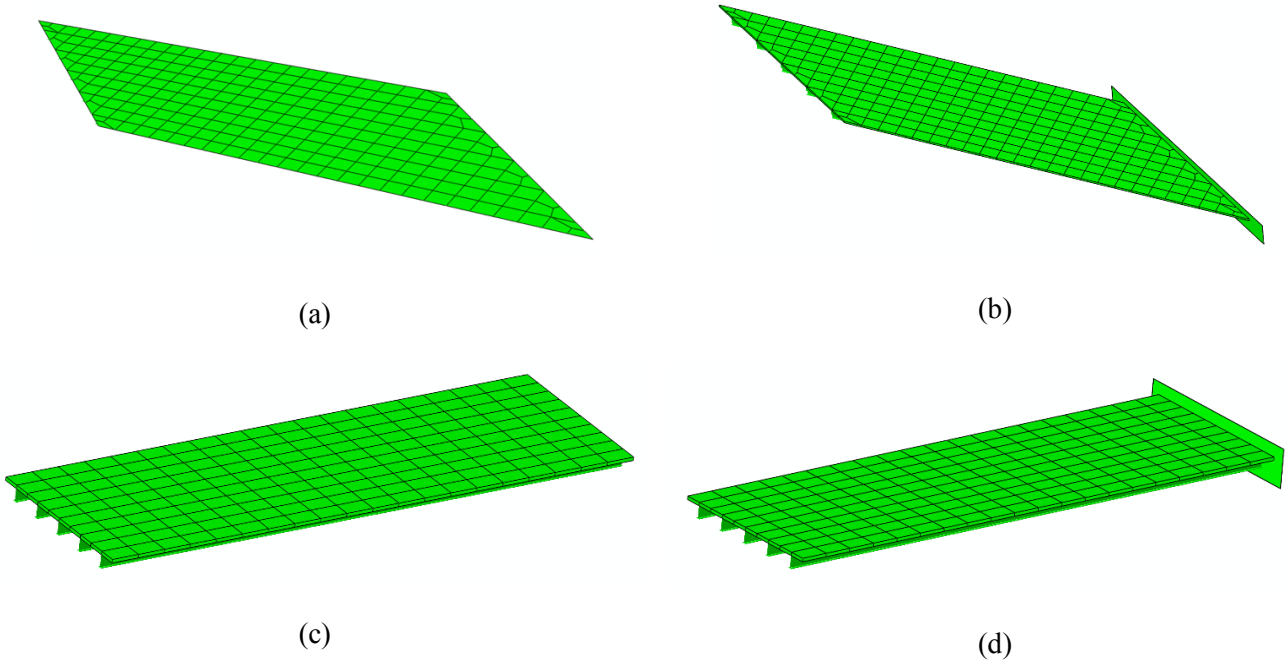

Figure 6. Skew models without (a) and with (b) abutment; and rectangular models without (c) and with (d) abutment.

4.3 MATERIAL PROPERTIES

The properties of carbon steel and concrete at ambient and elevated temperatures are defined according to the Eurocode values. The stress-strain curves are proposed as a function of temperature, in which the maximum yield stress of the steel at ambient was taken as 275MPa and the concrete has a maximum compressive strength of 30MPa.

The concrete constitutive behaviour is assumed to be consistent with the damaged plasticity and smeared crack model for slab and transverse diaphragms respectively in Abaqus. The tensile strength of the concrete was defined as 10% of the compressive strength with a minimum value of 0.1MPa. This may be deemed to be unrealistic as far as it allows the concrete slab to absorb more energy in tension than it would in a reality due to limited ductility. This issue should not overly affect the global response of the model as thermal strains act in a compensating manner to the tensile strains and enhance the available ductility.

4.4 BOUNDARY CONDITIONS

Simple rigid boundary conditions are used in the static analysis, and the support or foundation stiffness is not considered. According to the bridge drawings, the bearings at the west abutment are fixed, while the bearings at the central pier and the east abutment are free. Therefore, for the rectangular models, the primary beams were fully fixed in 5 degree of freedoms (DOFs) at the left support other than the rotation about the horizontal axis perpendicular to the longitudinal beam axis. At the middle and right support, the horizontal displacement and the same rotation are free while all other DOFs are restrained. The two ends of the concrete deck are also vertically constrained using roller supports, while there is no support defined at the middle support for the concrete slab because of its composite connection with the primary beams. For the skew models, boundary conditions are the same except that rotation is free about the longitudinal beam axis at all supports.

Composite action between the primary beams and concrete slab is achieved via multiple point constraints (MPCs). All nodes along the length of the beam and the corresponding slab nodes are so constrained. MPCs were also defined between the diaphragms and the slab to ensure that they acted as a single section in the transverse direction.

The influence of the expansion joint width has been partially studied in [14,15] for non-composite bridges with a small span (12.2m). In this paper, this effect is fully considered as the horizontal movement of the right support is expected to exceed the width of the expansion joint. Therefore a rigid surface is modelled using R3D4 elements to simulate the abutments, and is placed at a distance of 125mm from the right end of primary beams to model the free expansion joint gap. This type of element is used to provide a reaction to the superstructure when it impinges upon the abutment.

4.5 APPLIED LOADS

The applied loads include mechanical and thermal loads. In the mechanical part, transient loads such as the vehicular gravity load are not included based on the assumption that no vehicles would pass over the bridge when smoke and flames are visible below. The self-weight of beams, slab, parapet and pavement are considered as follows:

1) The self-weight of beams and slab are applied automatically through the defined dimensions with density of steel and concrete equal to 7850 kg/m^3 and 2400 kg/m^3.
2) Parapet: P1 type parapet which is a three-rail, cast-in post, steel parapet has a very small self-weight and therefore was neglected for the purposes of this paper.
3) Pavement: 100mm surfacing with hot rolled asphalt of 23kN/m^3 density [25], was applied as surface load in the Abaqus models.

Once the self-weight is applied, the thermo-mechanical analysis step commences. Since the central pier is a solid wall, the fire is considered to be intense within FAS when caused by a tanker accident. Therefore, this paper assumes the fire to be uniformly spread across FAS.

5. THERMO-MECHANICAL ANALYSIS OF BRIDGE MODELS

This section describes the response of the bridge models to a hydrocarbon fire with special consideration for the effect of abutment restraint. The analysis results are presented in various forms in order to gain useful insight into the fire resistance mechanisms of composite steel bridge superstructure. The following outputs (as indicated in Figure 5) are reported for both rectangular and skew bridge models to illustrate the response:

1) Deflection at the mid NFAS and FAS (Points A and B in Figure 5);
2) Horizontal displacement at right end pinned support (Point C in Figure 5);

3) Variation of deflection with time along NFAS;
4) Horizontal steel section force near middle and right support (Points D and E in Figure 5);
5) P-delta moment generated when the bridge impacts the abutment;
6) Vertical reaction force at all three supports;
7) Composite bending moment along both NFAS and FAS.

5.1 DEFINED PHASES OF BRIDGE STRUCTURAL RESPONSE

Progressive bridge damage is a dynamic process where the structure transits between alternative equilibrium paths. The structural response of the bridge during fire can be divided into the following three phases based on the change in flexural stiffness of the bridge structure and the effect of thermal bowing upon it:

1) Phase I: High flexural stiffness with low thermal bowing.
2) Phase II: Reduced flexural stiffness with increased thermal bowing.
3) Phase III: Impending global failure.

Phase I is the period where the temperature increases in FAS while the bridge stiffness remains largely unchanged. In this phase, the two spans are initially in sagging curvature because of the applied self-weight. Then, FAS deflects further downwards due to the increasing thermal gradient in the bridge structure which introduces a curvature resulting in thermal bowing ([26,27]). Meanwhile, NFAS deflects upwards to a maximum hogging (or negative) curvature enforced by the compatibility of deformation due to the continuity of the composite structure over the middle support. Horizontally, the free end in FAS displaces outwards due to thermal expansion.

Phase II is the period where thermal bowing increases together with strong reduction of stiffness. During this phase, FAS continues to deflect downwards at an increasing rate because of the reduced stiffness and

NFAS begins to deflect downwards after reaching a maximum hogging curvature also due to reduction of rotational stiffness over the middle support. The free end of FAS continues to displace horizontally outwards.

Phase III is the period where global collapse occurs. This phase starts when the outward horizontal displacement of the right ends of the beams begins to reverse. This can be considered to be the onset of global structural instability of the bridge. During this phase, the rate of deflection in FAS accelerates and runaway behaviour can be observed. NFAS continues to deflect in sagging curvature at a relatively steady rate. The following Table 1 describes the key structural features in each phase (as indicated in Figure 8).

	Curvature in FAS	Curvature in NFAS	Load redistribution	U1 reversal
Phase I	Sagging curvature	From sagging curvature to the maximum hogging curvature (or negative curvature)	FAS attracts more load	N/A
Phase II	Sagging curvature with an increasing rate of deflection	Reduction in hogging curvature	FAS begins to shed the overload	N/A
Phase III	Runaway deflection	Sagging curvature at a relatively steady state	Load redistributes from FAS to NFAS	Yes

Table 1. Key structural behaviours during fire.

5.2 RECTANGULAR MODELS

The deflected shape of the model with and without abutment at 20 min of fire are shown in Figure 7. This demonstrates that all composite primary beams have nearly identical behaviour resulting in a 'striped' pattern contour plot with maximum downward displacement near the middle of FAS. BEAM No.3 is therefore analysed and plotted in graphs as a representative beam.

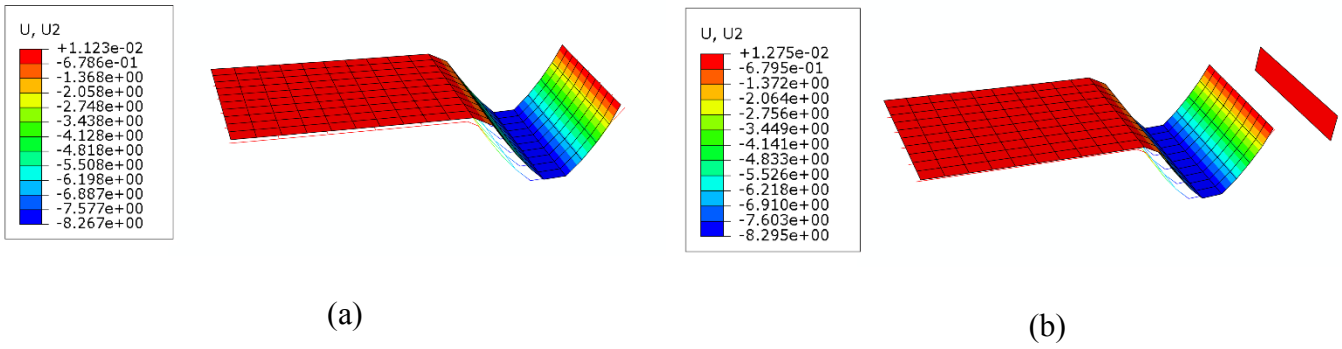

(a) (b)

Figure 7. Deformed rectangular model without (a) and with (b) abutment after 20 min of fire. All deflections are given in m.

Figure 8 compares the deflection history at mid FAS and mid NFAS with deflections beyond 2m not plotted for better observation of physical phenomena. The deflection behaviour is identical for both models in Phase I and Phase III showing that abutment has little effect on deflection during these phases. During Phase II, FAS in the model without abutment deflects downwards at an increasing rate due to thermal bowing. In the model with the abutment, NFAS has an additional upward deflection. This is because of the abutment restraint, inducing an increasing compressive force along the section. While FAS seems to deflect slower after impacting the abutment up to 10.3 min (Period A, shown in Figure 8). At the end of Period A, the model shows a sudden increase in deflection and then stabilises until the beginning of runaway collapse in Phase III (identified as Period B in Figure 8).

The phenomena seen in Period A and Period B can be explained by the P-delta effect (see Figure 11), which is derived from the eccentric horizontal reaction force at the abutment, located at the bottom of the steel section. During Period A, the neutral axis is above this resisting force, when the deflection in FAS is relatively small compared to the span length 24m (4%). This causes a hogging (negative) moment which acts against the increasing thermal bowing curvature. During Period B, the neutral axis moves below the abutment reaction force resulting in a sudden increase in deflection in FAS.

Figure 9 presents the horizontal displacement of free end during fire, it shows that displacement starts to change direction (inward) after 10.3 min when there is no abutment indicating the onset of collapse and after 11.7 min when the abutment exists. The deflected shapes along NFAS are also plotted in Figure 10 during the fire at key time points.

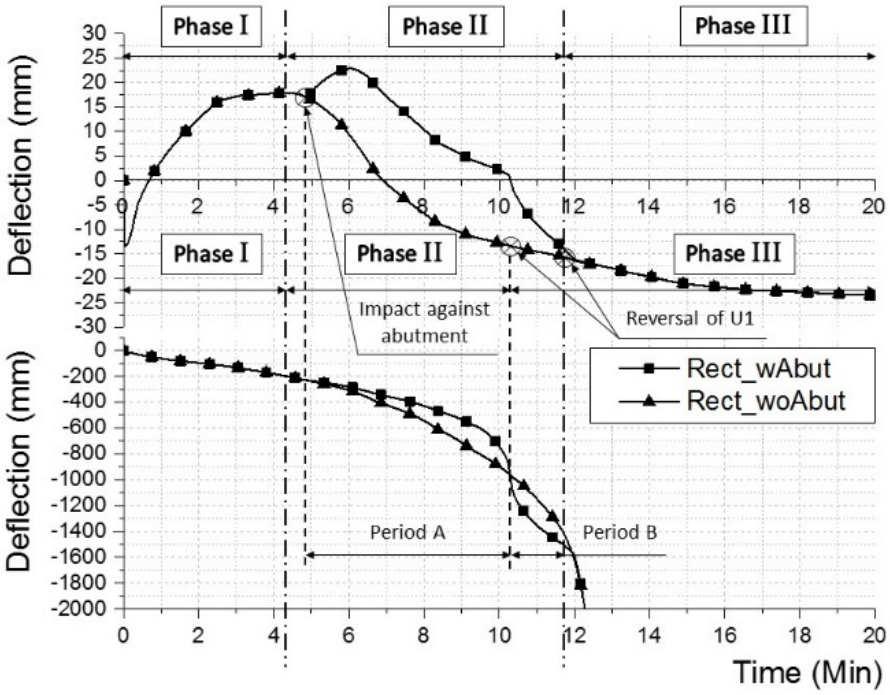

Figure 8. Comparison of the mid NFAS (top) and mid FAS (bottom) deflection variation with time.

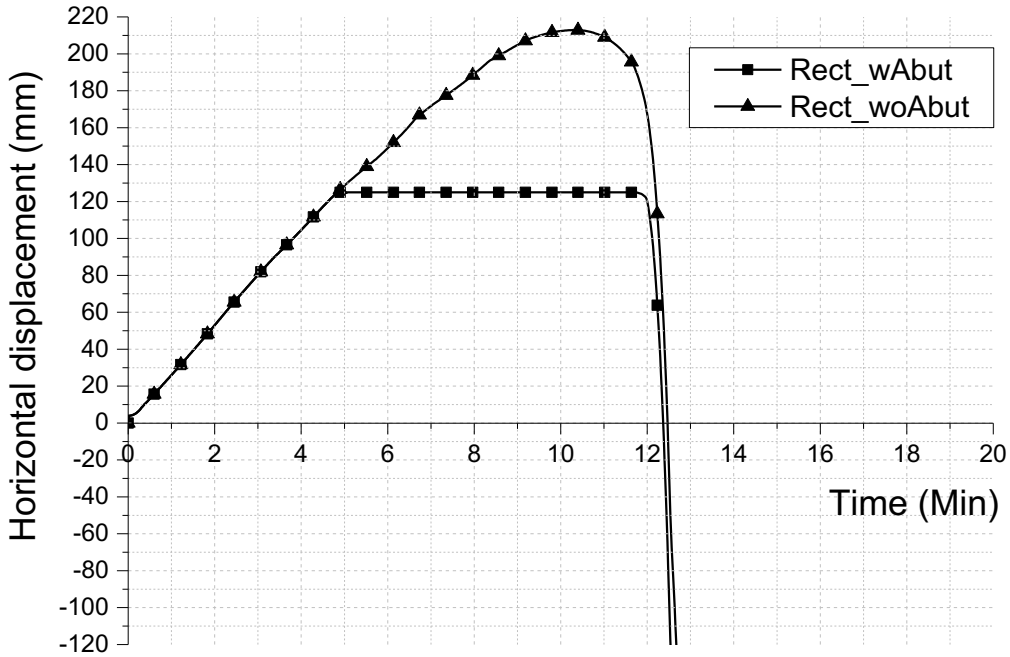

Figure 9. Comparison of the horizontal displacement at the right support.

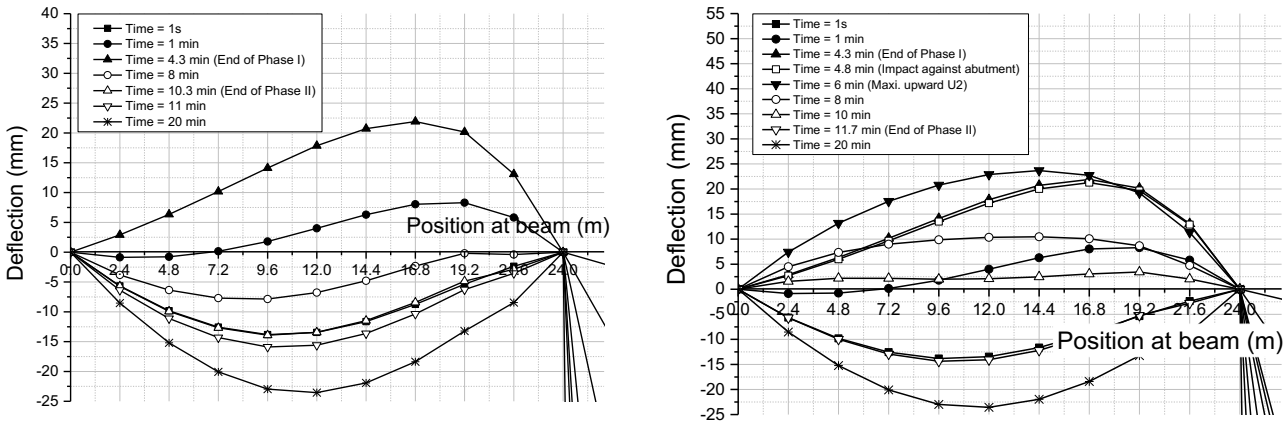

(a) (b)

Figure 10. Deflection along NFAS for the rectangular model without (a) and with (b) abutment.

Figure 12 illustrates the comparison of horizontal steel section force between the rectangular models. In Phase I, the composite connections, of hot steel section to the relatively cooler concrete slab, restrain the thermal elongation of steel beam creating compressive force along the beam and tensile force in the concrete slab. The compressive force in the steel section near middle support increases due to the additional hogging moment caused by the rotational restraint at the middle support and thermal bowing in FAS. During Phase

II, the steel section of the model without abutment attracts no further compression due to material degradation. While the model with abutment has an increasing compressive force derived from the thermal-expansion-induced abutment restraint force. At the end of Period A, the right support compressive axial force suddenly decreases because of the reversal of the P-delta moment (as shown in Figure 11).

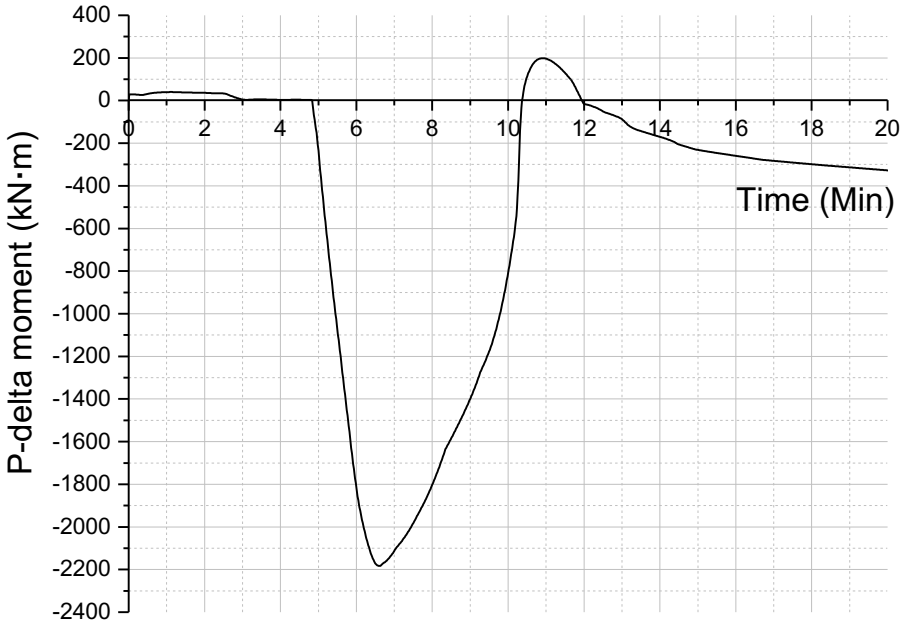

Figure 11. Change in P-delta moment with time in BEAM No.3 (Rectangular model with abutment).

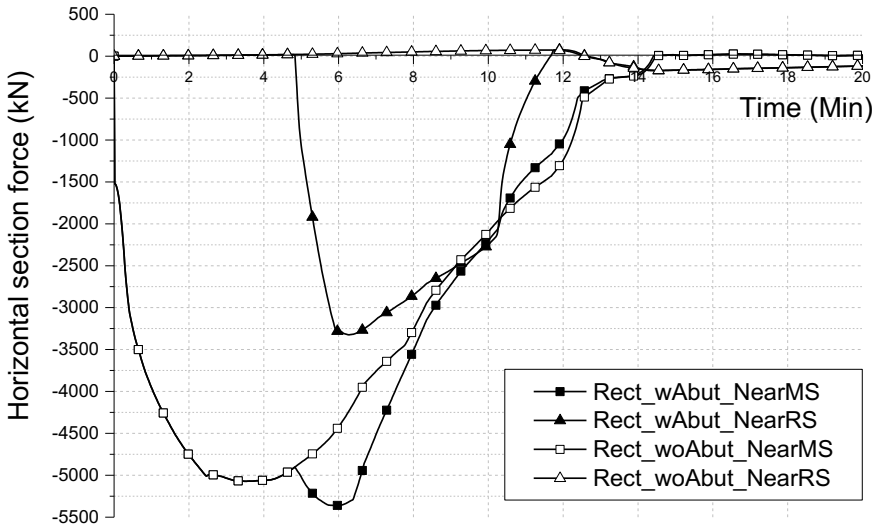

Figure 12. Comparison of horizontal steel section force near middle and right support.

Figure 13 plots the vertical reaction force at all three supports in BEAM No.3, where load redistribution can be observed. As observed earlier from the deflected shapes, all five beams are expected to show identical

behaviour, therefore results are shown only for the middle beam. Under the mechanical loading, the middle support takes greater load than the two end supports as expected. During Phase I, the vertical reaction force at the middle support increases because of the rotational restraint and increasing hogging moment. Meanwhile, the reaction force at the right support also increases because of the thermal bowing induced sagging curvature in FAS and the compatibility induced counter (hogging) curvature in NFAS, causing a pulling up force at the left support. Therefore, there is an overall redistribution of load from NFAS to FAS.

As discussed earlier, Phase II is dominated by the effect of reducing flexural stiffness of the bridge structure in FAS, which results in the reversal of the load redistribution from FAS to NFAS and as a result the reaction forces in the middle and right supports reduce while increasing at the left support. The model with abutment shows that lateral restraint induced at the right support prolongs the increase in vertical reaction at the right support and causes a load redistribution between the middle and right support, however the models coincide at the beginning of Phase III.

Figure 14 illustrates the composite bending moment along NFAS and FAS for the rectangular model with abutment. Assuming that the neutral axis lies at the interface of the steel beam and the reinforced concrete deck, the section forces in the beam and membrane forces in the slab can be used to estimate the composite bending moment.

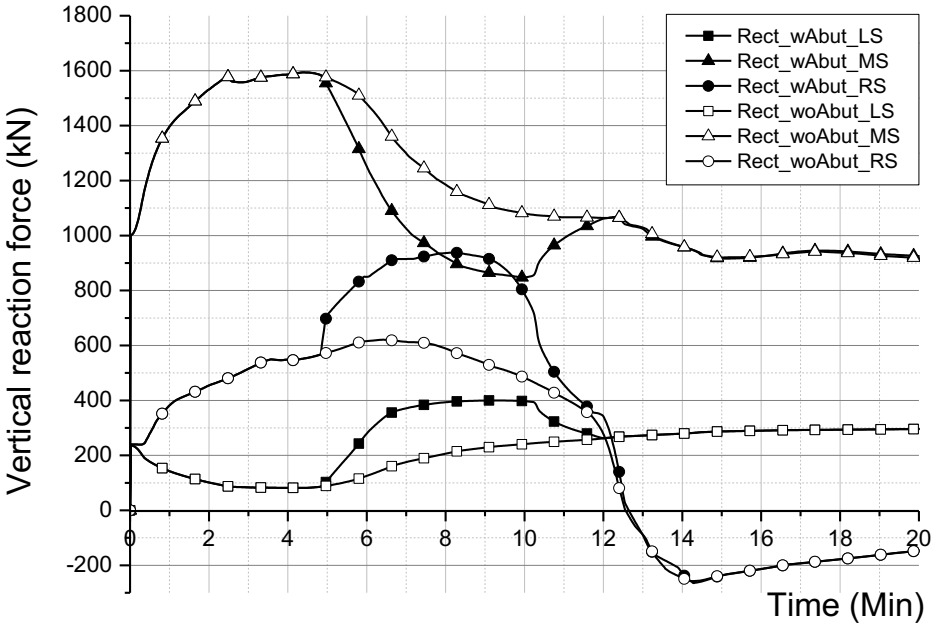

Figure 13. Comparison of change in vertical reaction force at supports with time.

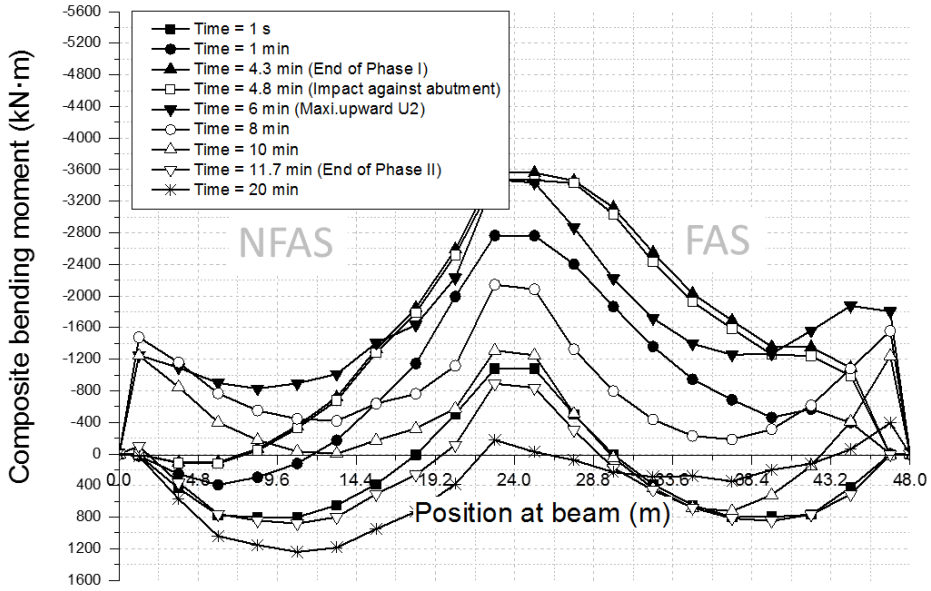

Figure 14. Composite bending moment variation with time along FAS and NFAS (rectangular model with abutment).

As shown in Figure 14, the maximum bending moment along FAS and above middle support is achieved at the end of Phase I (4.3 min). It then begins to reduce due to reducing stiffness in FAS in Phase II. The bending moment at middle support eventually reduces below the value resulting from the gravity loading

only, marking the end of Phase II and beginning of Phase III at 11.7 min. Load redistribution from FAS to NFAS can be seen clearly from this figure as well during both Phases II and III.

5.3 SKEW MODELS

Figure 15 shows that the beams in the skew models behave considerably differently from the rectangular models, resulting in a 'gourd' pattern contour plot and a clear two-way spanning behaviour which is captured by the model. The maximum downward deflection experienced is 0.54 m and 0.57 m for the model with and without abutment respectively, which are both located near the midpoint in BEAM No.5 (in the foreground). The two-way spanning action is apparently because of the difference in stiffness along the two diagonals in FAS, with the short diagonal showing stiffer behaviour resulting in a band of lower deflection along it.

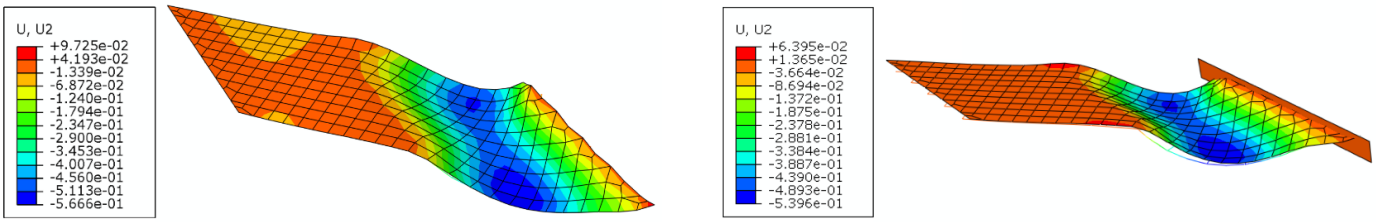

(a) (b)

Figure 15. Deformed skew models without (a) and with (b) abutment at 20 min (deformation scale factor 10). All deflections are given in m.

Figure 16 compares the deflection history between the two skew models at midpoint of NFAS and FAS for the most deflected beam (BEAM No.5). The figure also presents the deflection in NFAS for the other four beams in the model with abutment. It can be noticed that the durations of Phases I and II are almost identical in all beams. There is no sign of Phase III in the skew models, showing no horizontal displacement reversal or runaway failure.

The deflection history in NFAS shows that the initial stiffening of FAS, as seen in Phase I of the rectangular models, is also present in the skew models and lasts for about 4 min (as seen by the peak upward deflection in the NFAS of approximately 30 mm and 25 mm for the models with and without abutment). Also, as seen in the rectangular models the effect of reducing stiffness because of the elevated temperatures in FAS begins to govern the behaviour marking the beginning of Phase II.

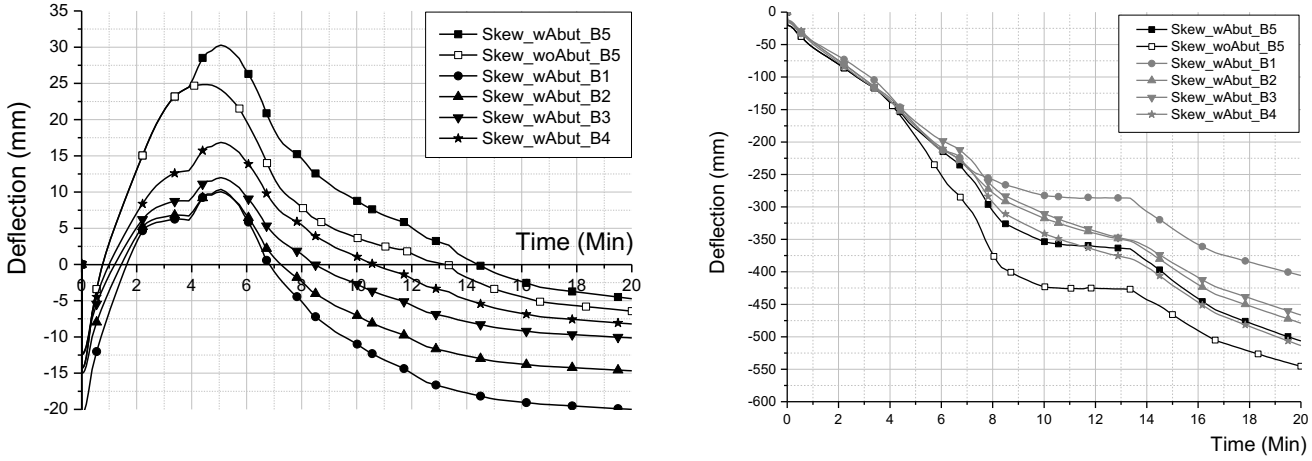

Figure 16. Comparison of the mid NFAS (a) and mid FAS (b) deflection variation with time.

Furthermore, as described in the context of Period A of the rectangular model, the skew model with abutment also shows lower deflections in FAS because of the negative P-delta moments induced by the abutment restraint. However, unlike the rectangular model there is no Period B in the skew model as the FAS deflections are not large enough to cause the reversal of the P-Delta moment.

Figure 17 shows the horizontal displacement history in all five beams of the skew models. The bottom flange of Beam No.5 impinges against the abutment first because of its greater deflection at around 4 min. The other beams follow and also impinge against the abutment restraint from BEAM No.4 at 4.9 min to BEAM No.2 at 7.83 min.

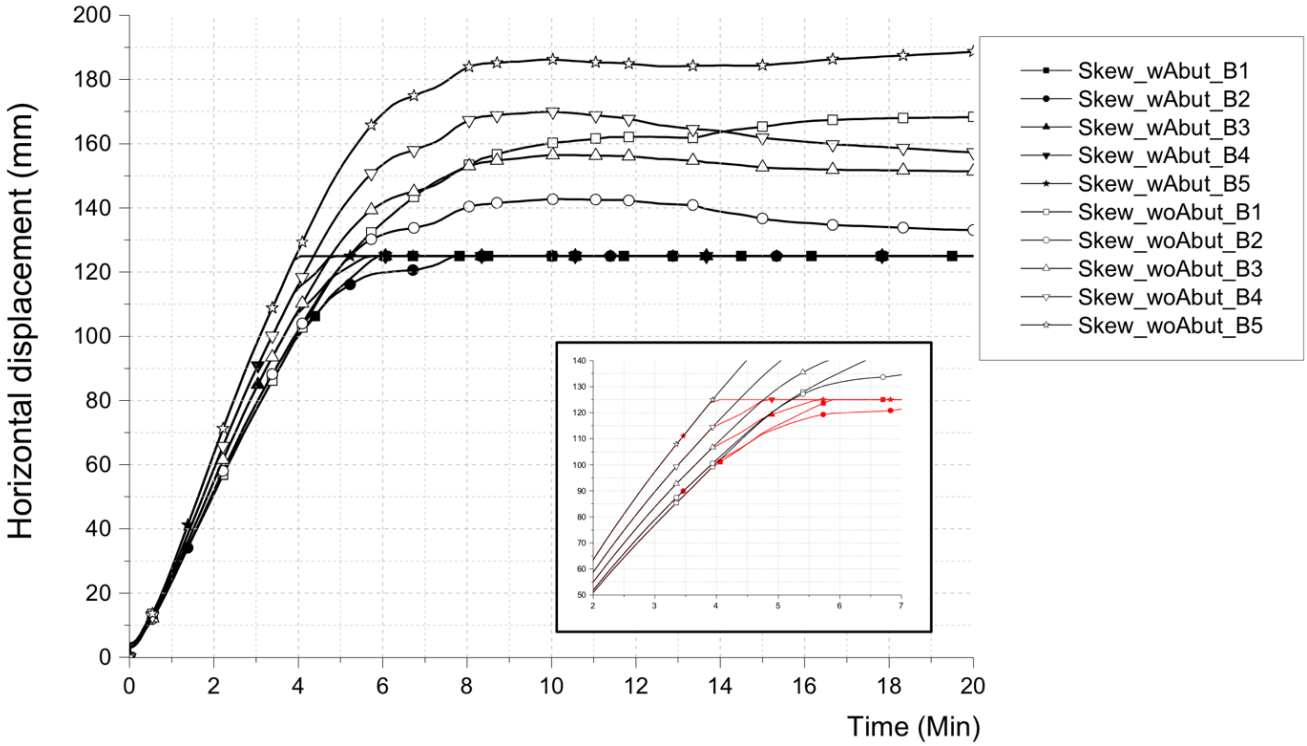

Figure 17. Comparison of the horizontal displacement at right support in all 5 beams between skew models (insert shows the details of first few min for clarity).

Figure 18 shows the variation of horizontal section force in FAS near right and middle support for the two skew models. For the skew model without abutment, only BEAM No.3 is plotted in Figure 18a as the representative of other three beams because of their nearly identical behaviour. Both skew models show identical behaviour in beam axial force at middle and right supports until approximately 4 min when BEAM No.5 impinges against the abutment. Figure 18a shows clearly the sequence of the impingent of each beam against the abutment, which corresponds to the sequence seen in Figure 17. As each beam impinges against the abutment, the section forces near the right support increase dramatically as shown by the deviation of the section force plots of the skew model without abutment.

In BEAM No.5, the section force is close to zero near the right support before impingement because the beam is not composite to the slab at the support points (as this results in the model being over-constrained).

The increasing section force in the other beams in FAS before impingement is due to their connection to the diaphragm beams, unlike BEAM No.5.

The section forces in beams near the middle support (Figure 18b) show a highly non-uniform distribution of forces within the structure in FAS, with the highest force in BEAM No.1 reducing sequentially to BEAM No.5 which has the lowest. This is likely to be the result of a complex interplay of factors, such as non-uniform deflections and two-way behaviour interacting with thermal bowing and the rotational restraint caused by structural continuity at the middle support. In the model with abutment the axial force generated in BEAM No.5 after impingement (Figure 18a) is distributed into the structure generating axial forces in all other beams, as shown in Figure 18b by the deviation from the plots of section forces. The magnitude of these deviations reduces with distance from BEAM No.5 with BEAM No.1 showing the least increase in section force at the middle support.

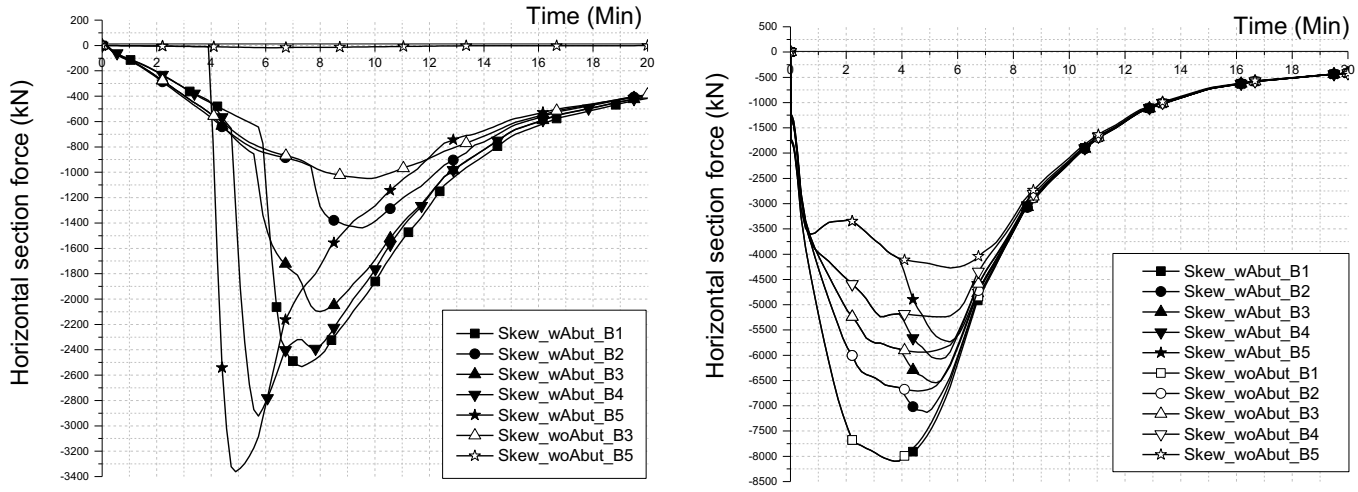

(a) (b)

Figure 18. Comparison of the horizontal section force near right (a) and middle (b) support.

As discussed earlier, the skew models have a two-way behaviour, therefore instead of plotting the deflections in NFAS for each beam, the deformation contour plots of the whole deck slab are shown in Figure 19 and the vertical reactions at all supports in both skew models are presented in Figure 20. When only gravity load is applied (Figure 19a), the end beams exhibit the most deflection: BEAM No.1 in NFAS

and BEAM No.5 in FAS. This is consistent with the vertical reaction force shown in Figure 20, where BEAM No.1 at the left support and BEAM No.5 at the right support take the least load, 68.56kN and 59.25kN respectively. The shorter diagonals of the bridge spans attract greater load because of their greater stiffness with BEAM No.5 at the left support and BEAM No.1 at the right support carrying an order of magnitude larger load with reactions of 586.91kN and 489.35kN respectively. The structure of the bridge model is anti-symmetric and this is reflected in the magnitudes of the initial vertical reaction forces at left and right supports. However, these reaction forces are not identical at corresponding points of anti-symmetry because of the nonlinear geometry used in the modelling. At the middle support, the vertical reactions at the locations of BEAM No.1 and BEAM No.5, due to the gravity load, are larger than at the locations of the middle three beams. This also reflects the higher stiffness of the short diagonal as in the case of the end supports.

During Phase I response to fire loading the stiffest part of the structure is the short diagonal in FAS (because of the added stiffness due to thermal deformation) and therefore it attracts a very large magnitude of the load, most of which goes to the right support at the location of BEAM No.1 (Figure 20a). The thermally induced curvature in FAS causes curling up along the long diagonal, resulting in negative reaction force in the right support at the location of BEAM No.5 and a reduced reaction at the middle support at BEAM No.1. The counter curvature in NFAS also produces a negative reaction at the left support at the location of BEAM No. 5 (Figure 20e).

In Phase II the short diagonal in FAS continues to attract greater load as the stiffness of the adjacent regions declines (Figure 20a). Load is also redistributed from FAS to NFAS as in the rectangular models but not as distinctly.

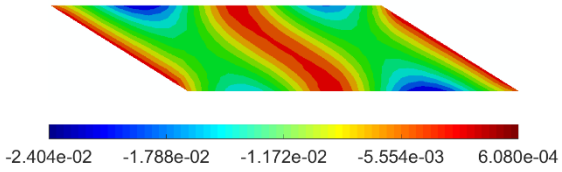

(a) Time = 1 s

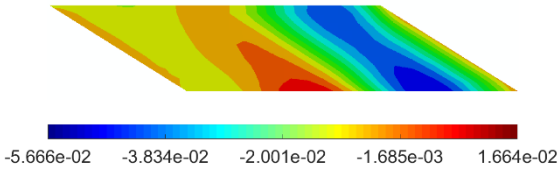

(b) Time = 1 min

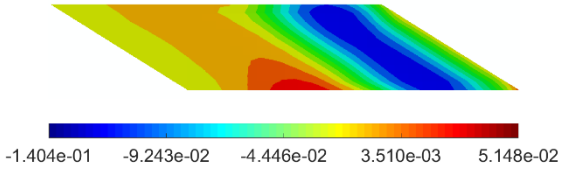

(c) Time = 4 min

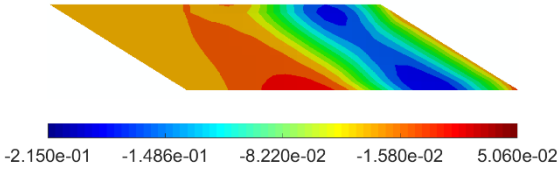

(d) Time = 5.4 min

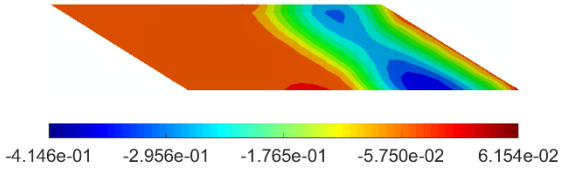

(e) Time = 9 min

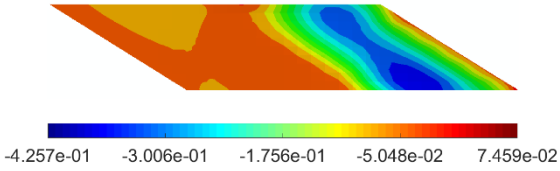

(f) Time = 12 min

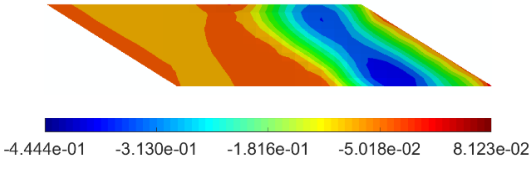

(g) Time = 14 min

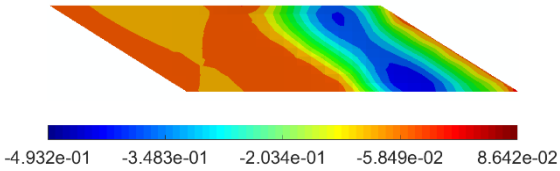

(h) Time = 15.73 min

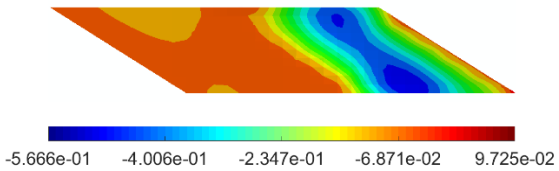

(i) Time = 20 min

Figure 19. The deflection (m) contours of the skew model without abutment.

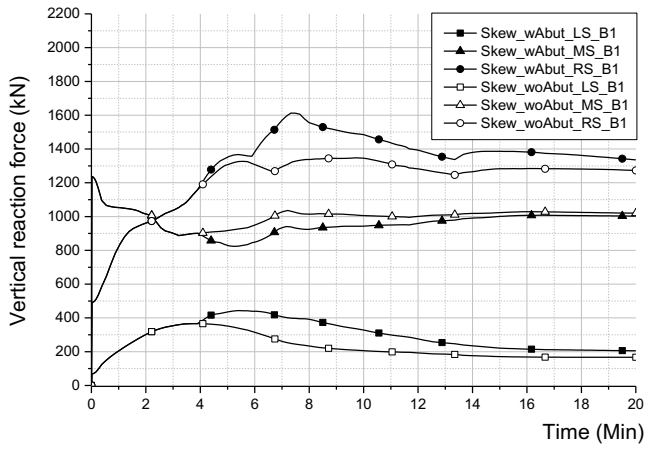

(a)

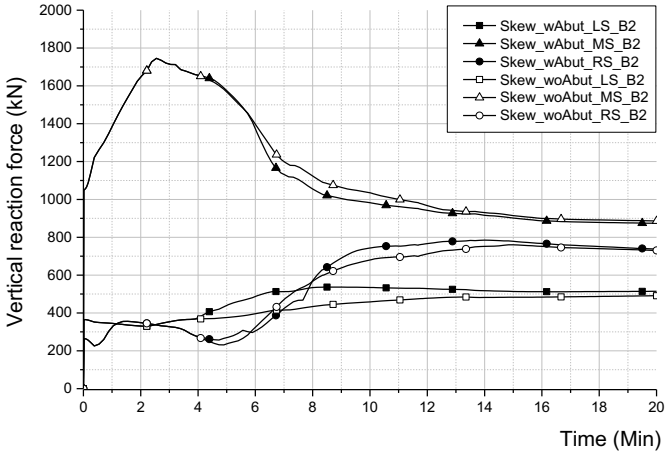

(b)

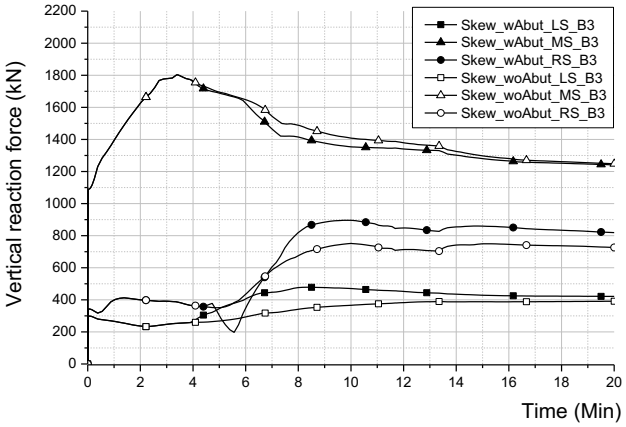

(c)

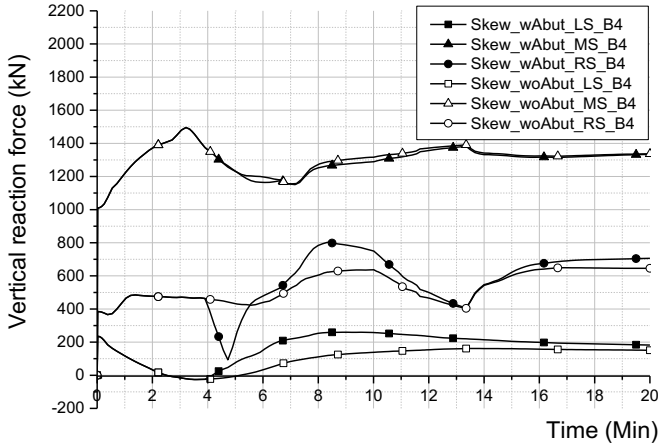

(d)

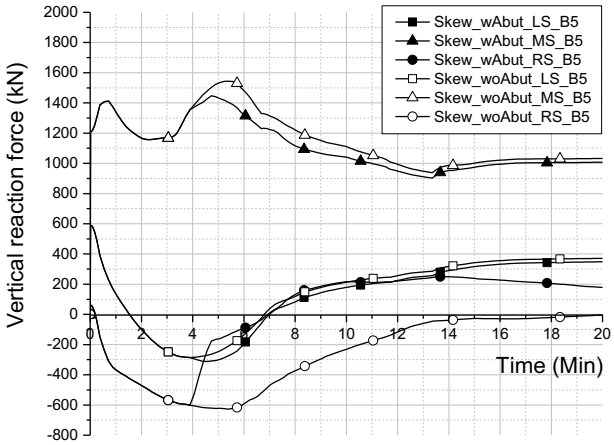

(e)

Figure 20. Comparison of vertical reaction force between skew models (a. BEAM No.1, b. BEAM No.2, c. BEAM No.3, d. BEAM No.4, e. BEAM No.5).

6. FAILURE ASSESSMENT

In this paper, the bridge is deemed to have failed if replacement of a girder or the deck would be required. The occurrence of failure is assumed as long as any one of the following conditions are fulfilled:

1) Runaway behaviour of deflection in the slab or beams.
2) Reversal of horizontal displacement at the free end-supports (east abutment support in this paper). This would suggest that the bridge span has softened to a point where the loads overcome the effect of thermal expansion [26,27] and the ends of the structure are pulled back towards the centre.
3) If the inward horizontal displacement at the free end exceeds the distance between bearing centreline and abutment edge (350mm in this case study), which will indicate that the superstructure has lost vertical support.
4) British Standards criteria [28]: a beam shall be regarded as failed if there is no capacity to support the test load which is determined if either of the following empirical criteria are exceeded:
   - A deflection of L/20;
   - The rate of deflection (in mm/min), calculated over 1 min intervals, on each min from the commencement of the heating period, exceeds the limit set by the following equation:

     Rate of deflection = L^2 / 9000d

     Where

     L is the clear span (mm) of specimen

     d is the distance (mm) from the top of the structural section to the bottom of the design tension zone

     NOTE. This rate of deflection limit shall not apply before a deflection of L/30 is exceeded.

Note that the code based failure criteria are based on standard furnace tests which do not account for the complex behaviour in a 3D bridge as illustrated in this paper. Therefore, the BS476 criterion is merely a reference and should not be considered as true indicator of failure.

Table 2 shows the failure time in each model based on each of the different criteria. The results from rectangular models with/without abutment show good agreement on the failure times between different criteria. According to the BS476 criterion, in rectangular models, if the deflection exceeds 1.2 m or the rate of deflection exceeds 45.71 mm/min (when the deflection is more than 0.8 m), failure could be considered to have occurred. If a conservative estimate is used, the rectangular models suggest that failure may occur around 10.6 min and 10.3 min in the model with and without abutment respectively. In the Hazel Park accident, collapse of the overpass occurred in about 20 min [1]. A failure time of around 10 min seems also reasonable in this case study as a very intense hydrocarbon fire uniformly engulfing the whole bridge span was used instead of a slower fire scenario.

Model	Reversal of horizontal displacement	Fall off from right abutment	British Standard: L/20	British Standard: Vertical deflection rate
Rectangular shape (with Abutment)	11.7 min	14.9 min	10.6 min	11.1 min
Rectangular shape (without Abutment)	10.3 min	13.0 min	11.2 min	10.4 min

Table 2. Comparison of the different failure criteria.

The skew shape seems to have a much more stable behaviour in fire with no failure. There is no indication of runaway or reversal of horizontal displacement and BS476 failure criteria of 1.44 m deflection or 65.83 mm/min are not reached either.

7. CONCLUSIONS

This research provides new insights in understanding of structural behaviour of bridges under vehicle fire loadings. The effect of skewness and the influence of abutment restraints on the overall fire performance of the bridge has been examined.

The failure assessments of structures in fire are generally based on deflection or rate of deflection criteria. Based on the investigation presented in this paper, the authors believe that the reversal of horizontal displacement at the free end is a more reliable indicator of runaway failure for non-skew shape bridges.

The skew bridge models manifest a much stiffer response to fire. Skew bridges would typically be safer in fire than non-skewed bridges, which is a significant finding for managers of bridge networks with limited funding for bridge maintenance. Inclusion of an abutment in the models does not affect the failure time significantly.

The hydrocarbon fire has limitations for application to bridges as it makes the bridge undergo rapid heating to 1000°C within a few min, which is perhaps too onerous a demand for bridges. A more bespoke fire would perhaps be more suitable based on a risk assessment including traffic flow information etc. Besides, the reduction of temperatures away from the burning vehicle is significant which was demonstrated by the first fire experiment of a bridge structure, conducted in 2017 [17]. In order to better understand the response of bridges subjected to fires, more realistic fire models should be used to take account of the decay fire intensity along the bridge span, none of which are captured by prescriptive curves.

No local failure is considered in this study. The connections in the model could possibly fail before global failure. Other local behaviour such as web buckling, shear connections and concrete spalling may also need

to be considered for a more rigorous investigation. In future work a risk assessment methodology would be proposed to evaluate the vulnerability of bridge network to vehicle fires. Guidance may be provided to improve the financial efficiency and reduce the potential fire risk.

ACKNOWLEDGEMENTS

A special thank you to Hazel McDonald of Transport Scotland, for providing drawings and a sincere thank you to Wayne Hindshaw and Nick Conroy (also of Transport Scotland) for the opportunity to present and discuss this work with them, and for their valuable advice. Thank you to Yanbin Xu for useful discussions during the initial stage of modelling.

REFERENCES

[1] V. Kodur, E. Aziz, M. Dwaikat, Evaluating fire resistance of steel girders in bridges, J. Bridg. Eng. 18 (2013) 633–643. doi:10.1061/(ASCE)BE.1943-5592.0000412.

[2] R.O. Carvel, A.N. Beard, P.W. Jowitt, D.D. Drysdale, Variation of heat release rate with forced longitudinal ventilation for vehicle fires in tunnels, Fire Saf. J. 36 (2001) 569–596. doi:10.1016/S0379-7112(01)00010-8.

[3] G. Flint, A. Usmani, S. Lamont, B. Lane, J. Torero, Structural Response of Tall Buildings to Multiple Floor Fires, J. Struct. Eng. 133 (2007) 1719–1732. doi:10.1061/(ASCE)0733-9445(2007)133:12(1719).

[4] D. Lange, C. Röben, A. Usmani, Tall building collapse mechanisms initiated by fire: Mechanisms and design methodology, Eng. Struct. 36 (2012) 90–103. doi:10.1016/j.engstruct.2011.10.003.

[5] S. Lamont, B. Lane, G. Flint, A. Usmani, Behavior of Structures in Fire and Real Design - A Case Study, J. Fire Prot. Eng. 16 (2006) 5–35. doi:10.1177/1042391506054038.

[6] Private Communication, Scotland Transerv, February 17, (2015).

[7] M. Garlock, I. Paya-Zaforteza, V. Kodur, L. Gu, Fire hazard in bridges: Review, assessment and

repair strategies, Eng. Struct. 35 (2012) 89–98. doi:10.1016/j.engstruct.2011.11.002.

[8] M. Davis, P. Tremel, A. Pedrego, Bill Williams River Concrete Bridge Fire Damage Assessment, Struct. Mag. (2008) 30–32.

[9] M.H. Ray, C.E. Carrigan, Final Report : Recommended Guidelines for the Selection of Test Levels 2 through 5 Bridge Railings, 2014.

[10] J. Hedden, M. Quagliata, T. Wandzilak, Emergency Renovation, Mod. Steel Constr. (2010).

[11] E.M. Aziz, V.K. Kodur, J.D. Glassman, M.E. Moreyra Garlock, Behavior of steel bridge girders under fire conditions, J. Constr. Steel Res. 106 (2015) 11–22. doi:10.1016/j.jcsr.2014.12.001.

[12] M. Naser, V. Kodur, Response of fire exposed composite girders under dominant flexural and shear loading, J. Struct. Fire Eng. (2017) JSFE-01-2017-0022. doi:10.1108/JSFE-01-2017-0022.

[13] E. Aziz, V. Kodur, An approach for evaluating the residual strength of fire exposed bridge girders, J. Constr. Steel Res. 88 (2013) 34–42. doi:10.1016/j.jcsr.2013.04.007.

[14] G. Peris-Sayol, I. Paya-Zaforteza, J. Alos-Moya, A. Hospitaler, Analysis of the influence of geometric, modeling and environmental parameters on the fire response of steel bridges subjected to realistic fire scenarios, Comput. Struct. 158 (2015) 333–345. doi:10.1016/j.compstruc.2015.06.003.

[15] I. Payá-Zaforteza, M.E.M. Garlock, A numerical investigation on the fire response of a steel girder bridge, J. Constr. Steel Res. 75 (2012) 93–103. doi:10.1016/j.jcsr.2012.03.012.

[16] J. Alos-Moya, I. Paya-Zaforteza, M.E.M. Garlock, E. Loma-Ossorio, D. Schiffner, A. Hospitaler, Analysis of a bridge failure due to fire using computational fluid dynamics and finite element models, Eng. Struct. 68 (2014) 96–110. doi:10.1016/j.engstruct.2014.02.022.

[17] J. Alos-Moya, I. Paya-Zaforteza, A. Hospitaler, P. Rinaudo, Valencia bridge fire tests: Experimental study of a composite bridge under fire, J. Constr. Steel Res. 138 (2017) 538–554. doi:10.1016/j.jcsr.2017.08.008.

[18] BEAR Scotland Ltd. Principal Inspection Report M9 8-8 10 - HILL O/B, 2011.

[19] B. Standard, Eurocode 1: Actions on Structures - Part 1-2: General Actions - Actions on Structures Exposed to Fire, (2002).

[20] BS EN 1992-1-2:2004, Eurocode 2: Design of concrete structures - Part 1-2: General rules - Structural fire design, (2004).

[21] BS EN 1993-1-2:2005, Eurocode 3: Design of Steel Structures - Part 1.2: General Rules - Structural Fire Design, (2005).

[22] J.-M. Franssen, V. Kodur, R. Zaharia, Designing Steel Structures for Fire Safety, CRC Press/Balkema, 2009.

[23] Abaqus 6.12 Benchmarks Manual, Abaqus 6.12. (2012).

[24] D. Iles, Determining the buckling resistance of steel and composite bridge structures, (2012). http://www.ihsti.com/CIS.

[25] B. Standard, Eurocode 1: Actions on Structures - Part 1-1: General Actions -- Densities, self-weight, imposed loads for buildings, (n.d.).

[26] A.S. Usmani, J.M. Rotter, S. Lamont, A.M. Sanad, M. Gillie, Fundamental principles of structural behaviour under thermal effects, Fire Saf. J. 36 (2001) 721–744. doi:10.1016/S0379-7112(01)00037-6.

[27] S. Lamont, B. Lane, A. Usmani, D. Drysdale, Assessment of the fire resistance test with respect to beams in real structures, Eng. J. 40 (2003) 63–75.

[28] BS 476-20:1987, Fire tests on building materials and structures - Part 20: Method for determination of the fire resistance of elements of construction (general principles), (1987).